Article:
Littlewood, JL, Shaw, S, Peacock, CL orcid.org/0000-0003-3754-9294 et al. (3 more authors) (2017) Mechanism of enhanced strontium uptake into calcite via an amorphous calcium carbonate (ACC) crystallisation pathway. Crystal Growth and Design, 17 (3). pp. 1214-1223. ISSN 1528-7483

https://doi.org/10.1021/acs.cgd.6b01599

Mechanism of enhanced strontium uptake into calcite via an amorphous calcium carbonate (ACC) crystallisation pathway

Janice L. Littlewood[1], Samuel Shaw[2], Caroline L. Peacock[1], Pieter Bots[2#], Divyesh Trivedi[3] and Ian T. Burke[1*]

[1]Earth Surface Science Institute, School of Earth and Environment, University of Leeds, Leeds, LS2 9JT, UK. *Corresponding Author's email: i.t.burke@leeds.ac.uk

[2]School of Earth and Environmental Sciences, University of Manchester, Manchester, M13 9PL, UK.

[3]National Nuclear Laboratories, Risley, Warrington, Cheshire, WA3 6AS, UK.

[#]Present address: Department of Civil and Environmental Engineering, University of Strathclyde, Glasgow, G1 1XJ, UK

Prepared for submission to *Crystal Growth and Design*.

Abstract

Calcite formation via an amorphous calcium carbonate (ACC) precursor phase potentially offers a method for enhanced incorporation of incompatible trace metals, including Sr^{2+}. In batch crystallisation experiments where $CaCl_2$ was rapidly mixed with Na_2CO_3 solutions the Sr^{2+} : Me^{2+} ratio was varied from 0.001 to 0.1; and, the pathway of calcite precipitation was directed by either the presence or absence of high Mg^{2+} concentrations (i.e. using a Mg^{2+} : total Me^{2+} ratio of 0.1). In the Mg-free experiments crystallisation proceeded via ACC → vaterite → calcite and average $K_{d\,Sr}$ values were between 0.44-0.74. At low Sr^{2+} concentrations (Sr^{2+} : Me^{2+} ratio ≤ 0.01) EXAFS analysis revealed that the Sr^{2+} was incorporated into calcite in the 6 fold coordinate Ca^{2+} site. However, at higher Sr^{2+} concentrations (Sr^{2+} : Me^{2+} ratio = 0.1), Sr^{2+} was incorporated into calcite in a 9-fold site with a local coordination similar to Ca^{2+} in aragonite, but calcite-like at longer distances (i.e. > 3.5 Å). In the high-Mg experiments the reaction proceeded via an ACC → calcite pathway with higher $K_{d\,Sr}$ of 0.90-0.97 due to the presence of Mg^{2+} stabilising the ACC phase and promoting rapid calcite nucleation in conjunction with higher Sr^{2+} incorporation. Increased Sr^{2+} concentrations also coincided with higher Mg^{2+} uptake in these experiments. Sr^{2+} was incorporated into calcite in a 9-fold coordinate site in all the high-Mg experiments regardless of initial Sr^{2+} concentrations, likely as a result of very rapid crystallisation kinetics and the presence of smaller Mg^{2+} ions compensating for the addition of larger Sr^{2+} ions in the calcite lattice. These experiments show that the enhanced uptake of Sr^{2+} ions can be achieved by calcite precipitation via ACC, and may offer a rapid, low temperature, low-cost, method for removal of several incompatible Me^{2+} ions (e.g. Pb^{2+}, Ba^{2+}, Sr^{2+}) during effluent treatment.

Introduction

Mechanisms of trace metal incorporation into calcium carbonate phases (e.g. calcite) have been the subject of scientific interest due to the use of trace element ratios in carbonate minerals for paleo-environmental reconstruction [1-3] and in dating techniques [4, 5]. It has also been proposed that divalent radionuclides (such as $^{60}Co^{2+}$ and $^{90}Sr^{2+}$) can be sequestered during subsurface *in* situ carbonate mineral formation offering a suitable route for limiting their migration at contaminated land sites [6-8]. In addition, *ex situ* effluent treatment technologies can utilise carbonate formation for radionuclide capture and long term safe storage in radioactive wastes [9, 10]. Indeed, the potential of carbonate precipitation for (*in situ* and *ex situ*) control of $^{90}Sr^{2+}$ has received much attention due to its importance in radioactive wastes (4.5% fission yield from ^{235}U), relatively long half-life (28.8 years), potential mobility in groundwater and radiotoxicity to humans [7, 8, 11, 12]. However, in order maximise the uptake of Sr^{2+} during carbonate precipitation and understand the factors which control Sr^{2+} incorporation during biomineralisation the mechanism and pathways of Sr^{2+} uptake during calcite crystallisation need to be determined at the molecular scale.

The three main anhydrous calcium carbonate polymorphs are calcite (β-$CaCO_3$), vaterite (μ-$CaCO_3$) and aragonite (λ-$CaCO_3$). The stable polymorph that occurs depends on solution chemistry, temperature and pressure during formation [2, 13]. Calcite is most stable at ambient conditions [14], and has a rhombohedral structure, consisting of layers of 6-fold coordinated Ca^{2+} ions, alternating with layers of carbonate ions [15]. Aragonite, generally forms at high pressure, and in the presence of higher aqueous concentration of Mg^{2+} and SO_4^{2-} [16], and has an orthorhombic crystal structure [15]. In aragonite, Ca^{2+} ions are 9 fold coordinated by oxygen in a hexagonal close packed arrangement [1]. The least stable polymorph at ambient conditions is vaterite [14]. There has been significant discussion of the crystal structure of vaterite, with recent studies indicating it is highly complex, consisting of a combination of 2-3 structures which can coexist within a pseudo-single crystal with Ca^{2+} ions that are 6-8 fold coordinated by oxygen [17-19].

The structures of the different calcium carbonate polymorphs have a significant control on the mechanism and degree of trace metal incorporation during crystal growth. A key factor controlling the uptake of Sr^{2+} in carbonate minerals is local coordination environment of Sr within the crystal structure. Sr in pure $SrCO_3$ is 9-fold coordinated, however Sr can be 6-fold coordinated on some carbonate phases (e.g. calcite). If Sr is substituted in 9 fold coordinated sites within calcium carbonate this leads to higher distribution coefficients than when incorporated in 6-fold coordinated sites. For example, due to its 6-fold Ca^{2+}-O coordination environment, trace metal distribution coefficients in calcite ($K_{d\ Me}$; the molar Me/Ca ratio in the solid $CaCO_3$ product as a function of the molar Me^{2+}/Ca^{2+} ratio in the solution from which it precipitated; see [20] and Eqn 3 below) for compatible elements (Me^{2+} ionic radius < Ca^{2+}; e.g. Mg^{2+}, Ni^{2+}) are orders of magnitude higher than for incompatible elements (Me^{2+} ionic radius > Ca^{2+}; e.g. Sr^{2+}, Pb^{2+}) [21, 22]. In contrast, aragonite, due to its larger 9-fold Me^{2+} coordination, more easily incorporates larger cations such as Sr^{2+}, with correspondingly higher $K_{d\ Sr}$ values [23]. K_d values also increase as a function of the observed crystal growth rate [24] which in turn is affected by a number of environmental factors, such as temperature, pH, ionic strength, the mechanism of formation and solution super saturation [2, 25, 26]. $K_{d\ Sr}$ values in the range 0.02-0.05 are commonly reported for Sr^{2+} incorporation into calcite by seeded inorganic growth mechanisms [20, 27, 28] although values up to 0.12-0.35 are reported when the crystallisation rate was increased [29].

In contrast, generally much higher $K_{d\ Sr}$ values are reported for Sr partitioning during calcite bio-mineralisation (e.g. 0.26-0.36 in experiments with coccoliths [30]; and 0.51-0.81 by earthworm-secreted calcium carbonate granules [31]). Biomineralisation processes often form via a short-lived, hydrated amorphous calcium carbonate (ACC) intermediate phase to control the morphology, mineralogy and physical properties of their final crystalline products [32]. In addition to higher $K_{d\ Sr}$ values, these bio minerals commonly have Mg : Ca ratios of >10 mol% Mg which is thought to be a result of high Mg^{2+} incorporation to the ACC precursor [33].

Sr^{2+}, despite being thought of as incompatible within the calcite structure [34], has recently been incorporated into calcite at high mol % ratios during the pressure induced crystallisation of an ACC precursor [21], although the mechanism of enhanced incorporation remains unclear. These results suggest that the crystallisation pathway also has a significant impact on Sr^{2+} uptake, with the carbonate formation via an amorphous precursor potentially significantly enhancing the levels of Sr^{2+} incorporation. In inorganic carbonate precipitation experiments, the thermodynamically unstable ACC precursor is achieved by adding excess carbonate ions to high molarity Ca^{2+} solution, often in a simple two solution mixing reaction [35]. This produces a solution highly oversaturated with respect to ACC allowing the metastable $CaCO_3$ polymorph to rapidly precipitate [36]. ACC then transforms within seconds to more stable polymorphs. At temperatures below 25 °C in the absence of other additives, the crystallisation pathway is ACC → vaterite → calcite [35, 37, 38]. In the presence of elevated Mg^{2+} concentrations (10% of the total Me^{2+} concentration) ACC transforms directly to calcite under the same reaction conditions [39]. The reaction end product is different at higher Mg^{2+} : Me^{2+} ratios. At 30% Mg^{2+}, ACC can transform to monohydrocalcite [40] and at 50% Mg^{2+}, the reaction end product is dolomite at elevated temperatures [41]. These pathways are in contrast to results from constant addition experiments where high Mg^{2+} : Ca^{2+} ratios typically favour aragonite formation [16]. However, aragonite is observed in ACC crystallisation experiments performed above room temperatures (> 40°C) [38], or where [Mg^{2+}] was in large excess of [Ca^{2+}] [42], or in the presence of high concentrations (50 % v/v) of ethanol [43].

Trace metal incorporation into ACC is not as selective as incorporation into crystalline materials, like calcite [44]. This is due to ACC's high surface area, poorly ordered structure and its rapid rate of formation [36]. The high uptake ratios of trace metals to ACC is then observed to be preserved in the crystallised end product (most often calcite) [45] despite experiencing a dynamic series of dissolution/precipitation reactions [37] that potentially offer an opportunity to selectively exclude larger ions (such as Sr^{2+}) that are incompatible in the calcite structure. Therefore, crystallisation of calcite via the ACC precursor offers a route to enhanced Sr^{2+} incorporation in calcite, and if achieved

at room temperature under simple reaction conditions may be the basis for a low cost capture method for contaminant $^{90}Sr^{2+}$ and other incompatible divalent contaminants.

The specific objective of this study was to determine if elevated Sr^{2+} concentrations can be sequestered into calcite, during low temperature crystallisation from an ACC precursor phase, via vaterite. In a separate series of experiments, Mg^{2+} was added to favour an alternative reaction pathway (not involving vaterite) to consider the effect of varying the reaction pathway and calcite composition on Sr^{2+} uptake. Finally, Sr K-edge EXAFS analysis was used to determine the precise nature of the Sr^{2+} incorporation mechanism as a function of reaction pathway and Sr^{2+} concentration during the crystallisation reaction .

Experimental

Carbonate precipitation experiments

Strontium and magnesium substituted calcium carbonates were crystallised by adding 10 mL aliquots of $MeCl_2$ solutions to 100 ml glass beakers containing 10 mL aliquots of Na_2CO_3 solution ($[Me^{2+}]$ and $[CO_3^{2-}]$ were equimolar in all experiments). Constant mixing was achieved using a Teflon coated magnetic stirrer bar and all experiments were performed in triplicate (or for selected experiments at six fold repetition) at room temperature (20 ±1°C). Six different Ca^{2+} dominated $MeCl_2$ solutions were used such that the molar ratio of Sr^{2+} : Ca^{2+} : Mg^{2+} was varied as described in Table 1, but that the total $[Me^{2+}]$ was maintained at 1.0 mol L^{-1}.

Table 1: Variation in the Ca^{2+} : Sr^{2+} : Mg^{2+} molar ratio used in carbonate precipitation experiments.

Experiment Description	**Volume $CaCl_2$ 1 mol L^{-1}**	**Volume $SrCl_2$ 1 mol L^{-1}**	**Volume $MgCl_2$ 1 mol L^{-1}**	**Volume Na_2CO_3 1 mol L^{-1}**
0.1 % Sr	9.99 mL	0.01 mL	-	10.00 mL
1 % Sr	9.90 mL	0.10 mL	-	10.00 mL
10 % Sr	9.00 mL	1.00 mL	-	10.00 mL
0.1 % Sr / 10 % Mg	8.99 mL	0.01 mL	1.00 mL	10.00 mL
1 % Sr / 10 % Mg	8.90 mL	0.10 mL	1.00 mL	10.00 mL
10 % Sr / 10 % Mg	8.00 mL	1.00 mL	1.00 mL	10.00 mL

In order to investigate the effect of initial solution concentration on carbonate precipitation kinetics and Sr^{2+} uptake, six additional experiments where preformed with $[Me^{2+}]$ of 0.1, 0.5 and 2.0 mol L^{-1} at 1% Sr (see SI Table S1-3 for details). In addition, a further set of four triplicate experiments investigated the effect of higher Sr^{2+} : Ca^{2+} molar ratios (15 - 75 % Sr^{2+}; see SI Table S4 for details). In selected experiments, Sr uptake to solids was monitored during carbonate crystallisation across a wide range of $[Me^{2+}]$ by additional of a $^{90}Sr^{2+}$ tracer (100 Bq mL^{-1}; 2.2 x 10^{-10} Mol L^{-1} as $SrCl_2$) to the initial $MeCl_2$ solution. During the carbonate precipitation process, 2 mL aliquots of solid suspension were recovered at intervals from < 30 seconds to 24 hrs, at which point the experiments were ended. The aqueous phase was separated by filtration (0.2 µm polycarbonate filters) and 1 mL was added to 10 mL EcoScintA scintillation cocktail (National Diagnostics Ltd., USA) prior to liquid scintillation counting (described below). Solid samples were only recovered from the experiments listed in Table 1 (and not

from the ^{90}Sr radiolabelled experiments; hence a 6 fold repetition of some experiments). At each sampling point, a 2 mL sample of the solid suspension was removed using a pipette, vacuum-filtered (0.2µm polycarbonate filters), quenched with isopropyl alcohol (IPA), dried at room temperature and stored in a desiccator prior to further characterisation (described below).

Aqueous and solid phase characterisation

All scintillation vials containing aqueous samples and cocktail were stored in the dark for 35 days (this allows for secular equilibrium to be established between ^{90}Sr and the ^{90}Y daughter product, and for any unsupported aqueous ^{90}Y present to decay below detection limits) and ^{90}Sr activity was determination by liquid scintillation counting using a Packard Tri-Carb 2100TR Liquid Scintillation Analyser (10 mins, 30-1020 keV). In all experiments, the fractional ^{90}Sr uptake (Q) to solids was calculated from the activities of ^{90}Sr in solution as follows:

$$Q = \frac{\mathrm{A_i - A_e}}{\mathrm{A_i}} \qquad (1)$$

Where A_i = initial added activity (Bq mL-1) and A_e = activity after precipitation. Further the fractional ^{90}Sr uptake can be used to calculate the molar distribution of strontium between the solid and aqueous phase as follows:

$$\mathrm{mol\ Sr_{(init)}} = V \times [\mathrm{Sr^{2+}}]_{\mathrm{(init)}} = (\mathrm{mol\ Sr_{(CaCO_3)}} \times Q) + (\mathrm{mol\ Sr_{(aq)}} \times (1 - Q)) \qquad (2)$$

Where V = the total solution volume. Finally, a strontium distribution coefficient ($K_{\mathrm{d\ Sr}}$) can be calculated that describes the molar Sr : Ca ratio in the bulk solid $CaCO_3$ in relation to the Sr^{2+} : Ca^{2+} ratio in the solution from which the $CaCO_3$ was crystallised [20]:

$$K_{\mathrm{d\ Sr}} = \frac{\mathrm{mol\ Sr_{(CaCO_3)}} \,/\, \mathrm{mol\ Ca_{(CaCO_3)}}}{[\mathrm{Sr^{2+}}]_{\mathrm{(init)}} \,/\, [\mathrm{Ca^{2+}}]_{\mathrm{(init)}}} \qquad (3)$$

Furthermore, as in these the experiments the initial $[Ca^{2+}]$ was high (0.1 – 2.0 mol L^{-1}) and the predicted solubility of relevant $CaCO_3$ phases (e.g. ACC, vaterite, calcite) is low (e.g. $K_{\mathrm{sp\ ACC}}$ = 4.0 x 10^{-7}; $K_{\mathrm{sp\ vaterite}}$ = 1.2 x 10^{-8}; $K_{\mathrm{sp\ calcite}}$ = 3.3 x 10^{-9}; all at 25 °C; [14, 46]) a near total (> 99.9 %) Ca^{2+} removal is expected, and therefore, mol $Ca_{(CaCO3)} \approx V$ x $[Ca^{2+}]_{(init)}$; i.e. the number of mol Ca^{2+} initially present.

Solid carbonate samples recovered from experiments were analysed by powder X-ray diffraction (XRD) using a Bruker D8 X-ray diffractometer, (Cu Kα radiation). Select calcite samples were analysed with the addition of a silicon internal standard (~20 % v/v) to allow accurate determination of unit cell volumes via Rietveld refinement of the whole XRD pattern using Topas 4-2 (Bruker, USA). The morphologies of precipitated crystallites was imaged using scanning electron microscopy (SEM). Samples were gold-coated (~20 nm) prior to analysis using secondary electron imaging on a FEI QUANTA 650 FEG environmental SEM operating a 10 keV using a 11 mm working distance.

X-ray absorption spectroscopy (XAS)

Sr K-edge (16,105 eV) X-ray analysis near edge structure (XANES) and Extended X-ray analysis fine structure (EXAFS) data was collected from selected solid samples recovered from the carbonate precipitation experiments detailed in Table 1. EXAFS spectra were collected during two separate beamtime sessions on beamline I18 at the Diamond Light Source, and beamline BM26A at the European Synchrotron Radiation Facility (ESRF). All samples were transported to the synchrotron as powders stored in desiccators, with the exception of samples representing very short reaction times (i.e. seconds – minutes), which were prepared freshly (using the same method as above) at beamline laboratories immediately prior to XAS analysis. All samples were prepared as pressed powder pellets (without diluent) and data was collected at 80 K using a liquid nitrogen cryostat. XAS data was summed and XANES spectra plotted using Athena v 0.8.056 ([47]). EXAFS data was background subtracted using PySpline ([48]), prior to fitting with DLexcurv v1.0 software ([49]; full details of beamline conditions and sample schedules can be found in SI section 1 and SI Table S5).

Results

Table 2 summarises the $CaCO_3$ phases determined in precipitation experiments as a function of time where $[Me^{2+}]$ = 1 mol L^{-1} (Example XRD patterns from the 1% Sr and the 1 % Sr / 10 % Mg experiments are shown in SI Figure S1). Two distinction crystallisation pathways were observed for experiments containing either high or no Mg^{2+} concentrations. For the Mg-free systems, a white gel-like precipitate of ACC formed rapidly in the supersaturated solution containing Ca^{2+}, Sr^{2+} and CO_3^{2-} ions. ACC has no distinctive XRD peaks but small peaks of vaterite were observed in patterns collected from samples recovered at the < 30 seconds time point. Vaterite was the major phase detected by 1 min and after 2 hours calcite was the dominant phase present. After 24 hours no vaterite was detected and calcite was the sole end product of the $CaCO_3$ crystallisation. In the high Mg^{2+} systems vaterite was not detected and XRD patterns collected at 5 mins did not contain any discernible peaks indicating the initial formation of ACC. After 4 hours calcite was detected which constituted the reaction end product observed at 24 hours. When the mole fraction of Sr^{2+} ions (as a % of the total Me^{2+} present) was greater than 10 %, strontianite was detected in the end product, which became the dominant end product of crystallisation where Sr^{2+} : Me^{2+} ratio was ≥ 50%. Calcite was the only mineral phase detected at 24 hrs in experiments where the $[Me^{2+}]$ was 0.1, 0.5 or 2.0 mol L^{-1}.

Table 2 Major and minor phases identified in XRD patterns collected from solid samples recovered from the $CaCO_3$ precipitation experiments described in Table 1 and SI Table S4 ($[Me^{2+}]$ = 1 mol L^{-1} in all experiments).

Experiment Description	Reaction Time	Major Phase detected	Minor phase detected
0.1 % Sr	<30 sec	ACC	vaterite
	1 min	vaterite	calcite
	2 hrs	calcite	vaterite
	24 hrs	calcite	-
1 % Sr	<30 sec	ACC	vaterite
	1 min	vaterite	calcite
	2 hrs	calcite	vaterite
	24 hrs	calcite	-
10 % Sr	<30 sec	ACC	vaterite
	1 min	vaterite	-
	2 hrs	calcite	vaterite
	24 hrs	calcite	-
0.1 % Sr / 10 % Mg	5 min	ACC	-
	4 hrs	calcite	-
	24 hrs	calcite	-
1 % Sr / 10 % Mg	5 min	ACC	-
	4 hrs	calcite	-
	24 hrs	calcite	-
10 % Sr / 10 % Mg	5 min	ACC	-
	4 hrs	calcite	-
	24 hrs	calcite	-
15 % Sr	24 hrs	calcite	strontianite
25 % Sr	24 hrs	calcite	strontianite
50 % Sr	24 hrs	strontianite	-
75 % Sr	24 hrs	strontianite	-

SEM images collected from the 1 % Sr and 1 % Sr / 10 % Mg systems (Fig. 1) illustrate the morphological changes observed during $CaCO_3$ crystallisation. In the Mg-free experiments clusters of nano-sized particles formed after a few seconds reaction time, this is consistent with previous SEM observations of ACC (e.g. [36, 50]) At 2 minutes spherulites of vaterite were observed. After 2 hours reaction, the images showed a mixture of calcite rhombohedra and vaterite spherulites. After 24 hours, only individual ~3-4 μm calcite rhombohedra were observed. In the high-Mg experiments, clusters of nano-sized ACC particles were observed in samples recovered at 5 minutes. After 2 hours, spherical aggregates of calcite crystallites were observed (typical for similar high-Mg experiments [42, 51]), which had crystallised as 5-10 μm clusters of ~1-2 μm rhombohedral calcite crystallites at 24 hours.

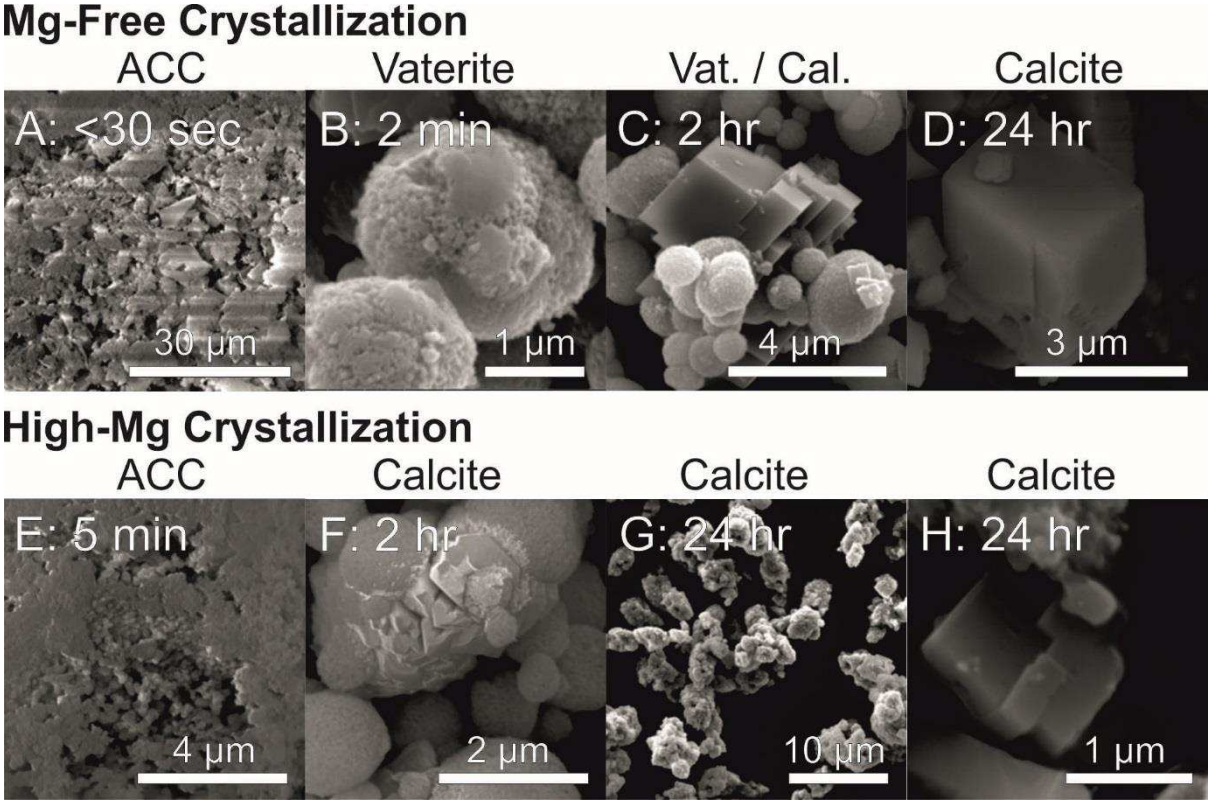

Figure 1. SEM photomicrographs showing the changes in crystallite morphology that occurred during A-D) the transformation of ACC → vaterite → calcite in the Mg-free experiments (1 % Sr) and E-F) the transformation of ACC → calcite in the high-Mg experiments (1 % Sr: 10 % Mg). (The horizontal stripes shown in panel A are an artefact due to surface charging in the electron microscope.)

There was a significant difference in Sr uptake ($K_{d\ Sr}$) between the high-Mg and Mg-free crystallisation experiments (Fig. 2) with much higher $K_{d\ Sr}$ values determined for the high-Mg experiments ($K_{d\ Sr}$ = 0.90-0.97 and 0.44-0.74 respectively; this equates to an observed Sr^{2+} removal of 50-80 % in the Mg-free experiments and 90-100 % in the high-Mg experiments; see SI Figure S2 and S3 for details). For the [Me^{2+}] = 1 mol L^{-1} experiments, there was no significant trend in $K_{d\ Sr}$ values determined as either a function of reaction time (Fig. 2a), or, mole fraction Sr^{2+} present in the initial solution (Fig 2b). There was, however, an observed trend of increased $K_{d\ Sr}$ in the Mg-free experiments with increased total [Me^{2+}] in the initial solution (Fig. 2c); a small discernible increasing trend was also observed in the High-Mg experiments.

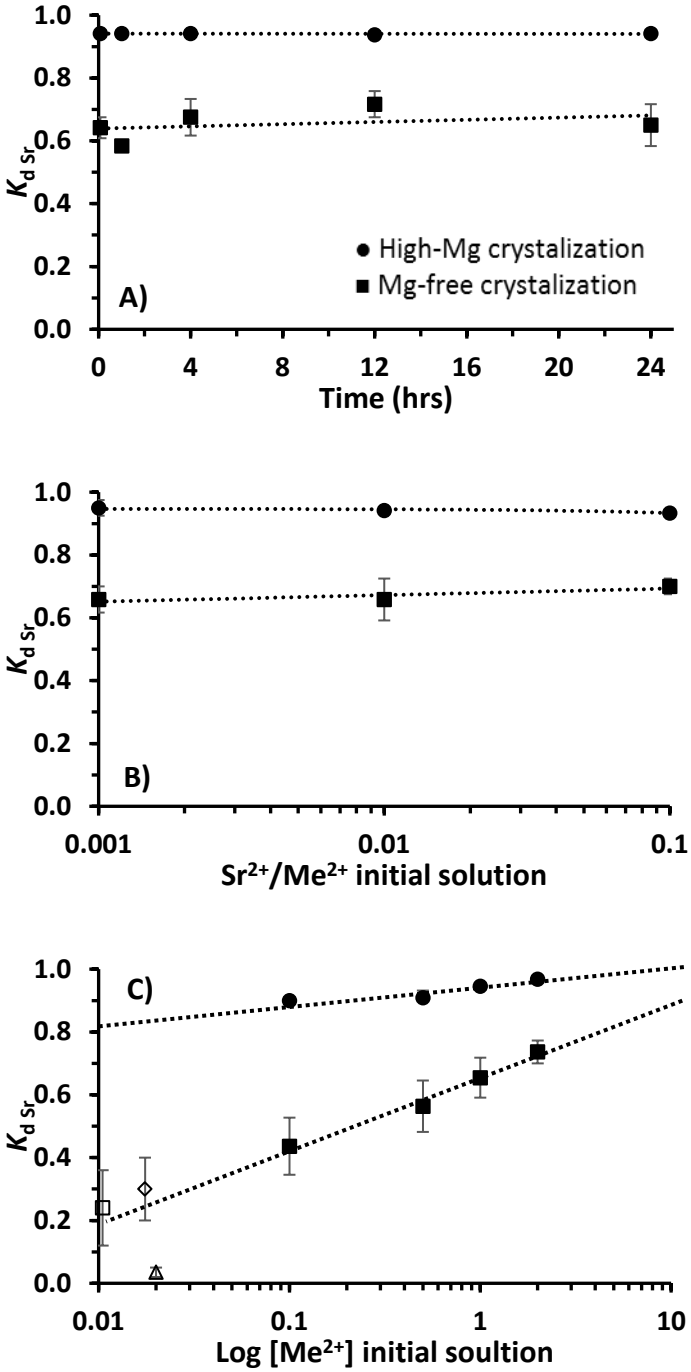

Figure 2. Change in $K_{d\ Sr}$ determined in crystallisation experiments as a function of: A) reaction time; B) mole fraction of Sr^{2+} present in the initial solution ($[Me^{2+}]$ = 1 mol L^{-1}; 24 hr time point), and; C) the total $[Me^{2+}]$ present in initial solutions (Sr^{2+} : Me^{2+} = 0.01; 24 hr time point). Error bars are ±1 σ of triplicate experiments and where not shown are smaller than the size of the symbols used. Dashed best fit lines are added to guide the eye. Open triangle indicates the range of equilibrium $K_{d\ Sr}$ determined in constant addition experiments at low crystal growth rates (<0.01 mmols L^{-1} day^{-1}; [20]). Other open symbols represent range of $K_{d\ Sr}$ determined in calcite precipitation experiments preformed with elevated crystal growth rates (0.1-0.3 mmols L^{-1} day^{-1}; [29, 52]).

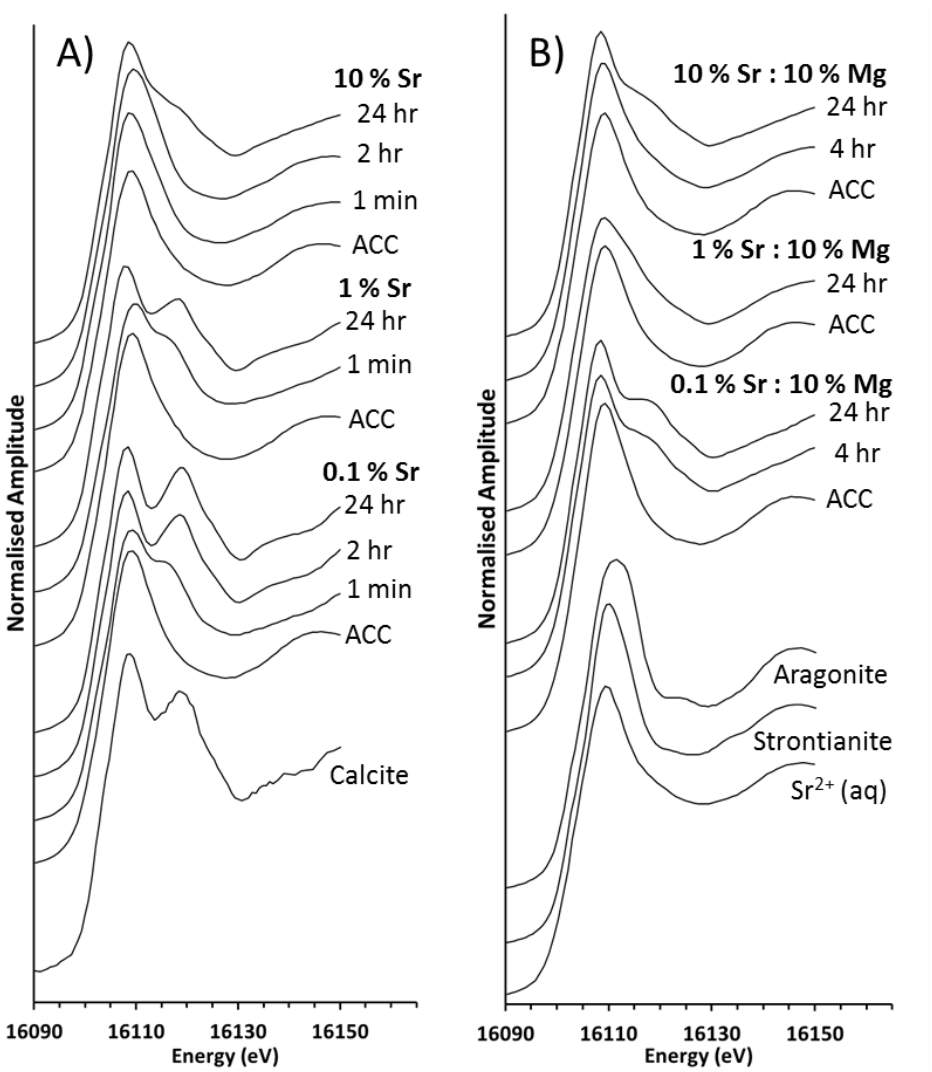

Figure 3. Sr K-edge XANES spectra collected from selected calcium carbonate samples recovered from A) Mg-free, and B) high-Mg, crystallisation experiments ([Me^{2+}] = 1 mol L^{-1}) with data collected from selected Sr^{2+} containing standards.

Sr K-edge XANES data collected from selected calcium carbonate samples recovered from the crystallisation experiments (Fig. 3) show clear changes as a function of reaction time in all experiments. The initial spectra collected at the shortest reaction times contain features that are very similar to the spectra collected from a $Sr^{2+}_{(aq)}$ solution (i.e. a single 'white line' peak present at ~16,108 eV). After longer reaction times, the spectra collected show increased complexity and a second peak is clearly discernible in XANES spectra at ~16,118eV. This is most apparent for the 24 hr samples from the 0.1% Sr, 1% Sr and 0.1 % Sr: 10% Mg experiments (this is characteristic for Sr in 6 fold coordination within the calcite structure [53]). None of the end product Sr^{2+} XANES spectra are well matched by the

spectra collected from the strontianite or aragonite standards. Background subtracted EXAFS spectra collected from the same samples (Fig. 4) also follow the general pattern of increasing complexity as a function of increasing reaction time. EXAFS data from freshly precipitated ACC samples are essentially identical to the $Sr^{2+}_{(aq)}$ sample and can be best fit with a single shell of ~8 O atoms at 2.60 ±0.02 Å (Table 3). Samples recovered from the Mg-free experiments after short reaction times (i.e. 1 min) contained vaterite and their EXAFS spectra were fitted with ~8 O atoms at 2.55 ±0.03 Å, ~5 C atoms at 3.1 ±0.1 Å and ~3 Ca atoms at 4.22 ±0.05 Å. After 24 hrs calcite was the end product of the crystallisation reactions, and for the Mg-free experiments with low Sr loadings (0.1% Sr and 1% Sr experiments) the Sr EXAFS spectra were fitted with four shells of backscatters corresponding to ~6 O atoms at 2.50 ±0.01 Å, ~6 C atoms at 3.35 ±0.1 Å, ~6 Ca atoms at 4.11 ±0.05 Å and ~6 Ca atoms at 5.01 ±0.05 Å. The best fit for EXAFS spectra collected from calcite samples from the experiments with high Sr loading (10% Sr) and the three High-Mg experiments were different. For these samples the data was best fit with three shells of backscatters including ~9 O at 2.55 ±0.03 Å, ~5 C atoms at 3.1 ±0.1 Å and ~5 Ca atoms at 4.10 ±0.05 Å.

Figure 4. Sr K-edge EXAFS spectra collected from selected calcium carbonate samples recovered from high-Mg and Mg-free crystallisation experiments ($[Me^{2+}]$ = 1 mol L^{-1}) and corresponding Fourier transformations. Dashed lines represented best fits to the data calculated in DLexcurv.V1.0 using the parameters given in Table 3.

[For Figure 4 see next page]

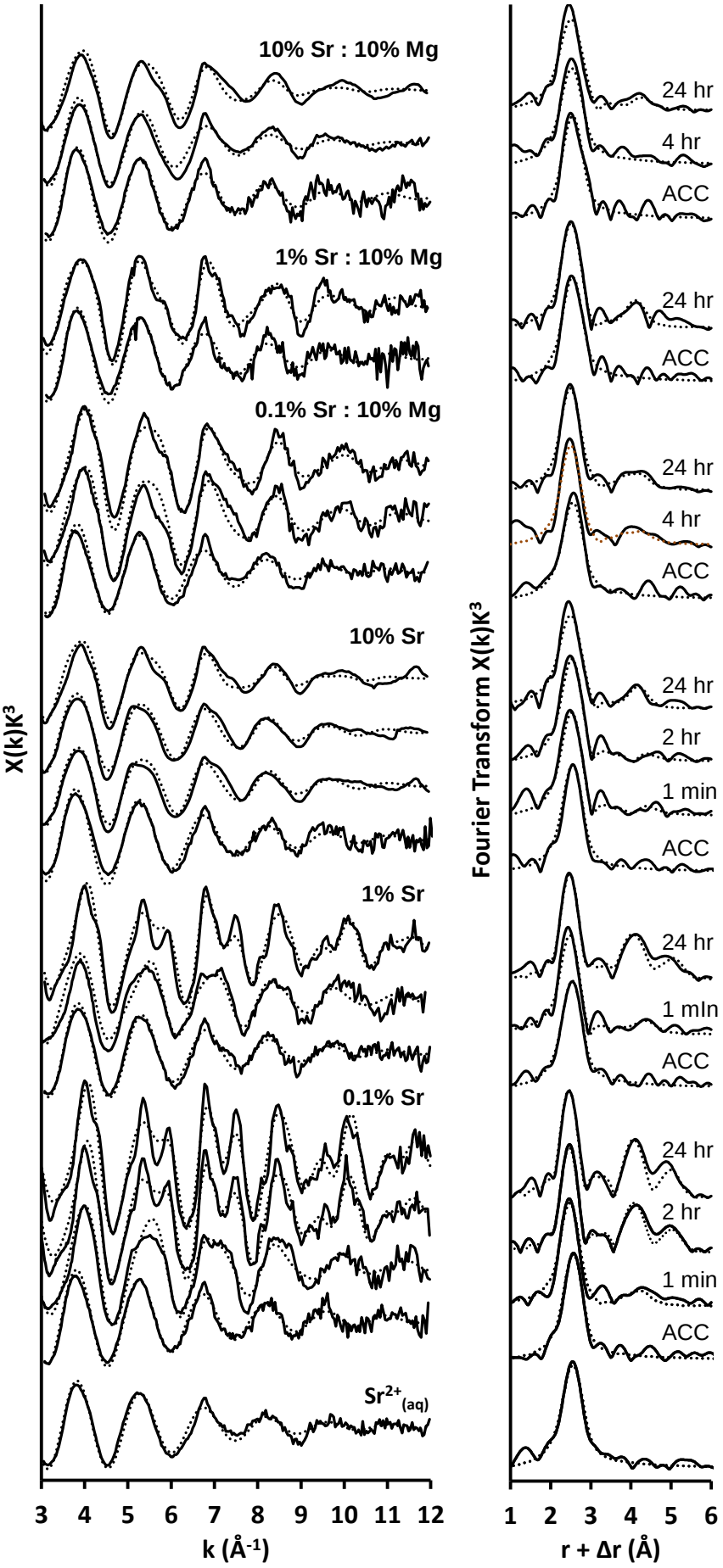
10% Sr : 10% Mg
1% Sr : 10% Mg
0.1% Sr : 10% Mg
10% Sr
1% Sr
0.1% Sr
Sr2+(aq)
X(k)K3
3 4 5 6 7 8 9 10 11 12
k (Å-1)
24 hr
4 hr
ACC
24 hr
ACC
24 hr
4 hr
ACC
24 hr
2 hr
1 min
ACC
24 hr
1 mIn
ACC
24 hr
2 hr
1 min
ACC
Fourier Transform X(k)K3
1 2 3 4 5 6
r + Δr (Å)

Table 3 Sr K-edge EXAFS fits, where N is the Occupancy (±25%; only whole number fits used), r is the interatomic distance, $2\sigma^2$ is the Debye–Waller Factor and χ^2 is the goodness of fit parameter. Uncertainties in the last digit shown in parentheses.

Experiment Description	Reaction Time (1° phase)	Shell	N	r (Å)	$2\sigma^2$ (Å^2)	χ^2
0.1 % Sr	ACC	O	8	2.60(2)	0.024(6)	2.75
	1 min	O	8	2.52(2)	0.022(6)	4.17
	(vaterite)	C	4	3.1(1)	0.05(1)	
		Ca	4	4.19(5)	0.029((7)	
	2 hrs	O	6	2.50(2)	0.011(3)	5.47
	(calcite)	C	6	3.4(1)	0.032(8)	
		Ca	6	4.10(5)	0.016(4)	
		Ca	6	5.00(5)	0.019(5)	
	24 hrs	O	6	2.49(2)	0.010(3)	4.62
	(calcite)	C	6	3.3(1)	0.024(6)	
		Ca	6	4.09(5)	0.013(3)	
		Ca	6	5.02(5)	0.015(4)	
1 % Sr	ACC	O	8	2.58(2)	0.027(7)	2.85
	1 min	O	8	2.55(2)	0.023(6)	9.15
	(vaterite)	C	6	3.0(1)	0.04(1)	
		Ca	4	4.27(5)	0.035(9)	
	24 hrs	O	6	2.51(2)	0.014(4)	4.55
	(calcite)	C	6	3.4(1)	0.06(2)	
		Ca	6	4.10(5)	0.019(5)	
		Ca	6	5.00(5)	0.021(5)	
10 % Sr	ACC	O	8	2.59(2)	0.027(7)	3.14
	1 min	O	8	2.58(2)	0.030(8)	4.07
	(vaterite)	C	4	3.0(1)	0.033(8)	
		Ca	2	4.19(5)	0.04(1)	
	2 hrs	O	8	2.59(2)	0.028(7)	3.35
	(calcite)	C	4	3.0(1)	0.037(9)	
		Ca	2	4.18(5)	0.04(1)	
	24 hrs	O	9	2.57(2)	0.035(9)	4.55
	(calcite)	C	5	3.1(1)	0.04(1)	
		Ca	4	4.12(5)	0.036(9)	
0.1 % Sr : 10 % Mg	ACC	O	8	2.60(2)	0.029(7)	2.73
	4 hrs	O	9	2.54(2)	0.023(6)	6.64
	(calcite)	C	5	3.1(1)	0.04(1)	
		Ca	6	4.11(5)	0.04(1)	
	24 hrs	O	9	2.52(2)	0.023(6)	3.63
	(calcite)	C	4	3.1(1)	0.04(1)	
		Ca	6	4.10(5)	0.035(9)	
1 % Sr : 10 % Mg	ACC	O	8	2.59(2)	0.026(7)	4.65
	24 hrs	O	9	2.56(2)	0.023(6)	5.54
	(calcite)	C	5	3.0(1)	0.04(1)	
		Ca	6	4.06(5)	0.033(8)	
10 % Sr : 10 % Mg	ACC	O	8	2.59(2)	0.026(7)	4.27
	4 hrs (calcite)	O	8	2.57(2)	0.033(8)	3.74
	24 hrs	O	9	2.56(2)	0.035(8)	6.00
	(calcite)	C	4	3.1(1)	0.037(9)	
		Ca	4	4.12(5)	0.04(1)	
$Sr^{2+}_{(aq)}$	-	O	8	2.60(2)	0.030(8)	3.14

Calcite unit cell volumes calculated from the XRD patterns (Fig. 5.) show that samples recovered after 24 hrs from the Mg-free experiments, the volume was similar to pure calcite (367.8 $Å^3$; [45]) at low Sr contents, and increased as a function of increasing Sr loading. For the calcite samples recovered from the High-Mg experiments, the unit cell volumes were significantly lower than pure calcite and showed a decreasing trend with increased Sr-loading.

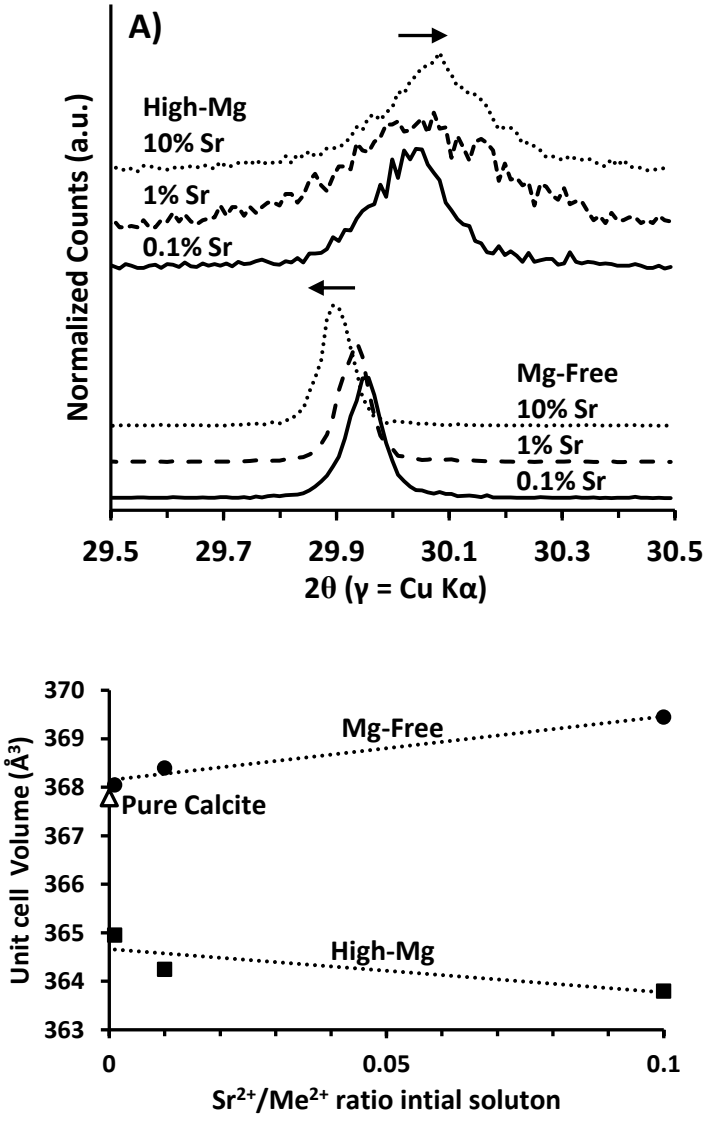

Figure 5. A) XRD patterns showing detailed view of the silicon calibrated and normalized 100 calcite peaks collected from selected high-Mg and Mg-free crystallization experiments after 24 hrs reaction time (total $[Me^{2+}]$ = 1 mol L^{-1}); and B) Corresponding lattice volumes calculated from the XRD traces. Dashed best fit lines are added to guide the eye. Open triangle indicates measured value for pure calcite from reference [45].

Discussion

Effect of Sr^{2+} and Mg^{2+} on calcium carbonate crystallisation

The reaction pathway observed during the precipitation of calcium carbonate via ACC in experiments amended with Sr^{2+} ions was the same as that observed for the formation of pure calcium carbonate; namely, an extremely rapid precipitate of ACC, transformation to vaterite within minutes and finally recrystallisation to calcite within 24 hours [36]. Strontianite was first detected as a reaction product when the initial Sr^{2+} / Me^{2+} ratio was greater than 0.1, and at Sr^{2+} / Me^{2+} ratios > 0.25 strontianite was the dominant reaction product. Thus, the complete substitution of Sr^{2+} into calcium carbonates via ACC precipitation was found to be limited to initial solutions with Sr^{2+} / Me^{2+} ratios < 0.1 (also as observed by [21]).

The presence of high concentrations of Mg^{2+} ions in addition to Sr^{2+} resulted in a different reaction pathway. The presence of high Mg^{2+} concentrations (Mg^{2+} / Me^{2+} = 0.1) favours the formation of calcite over vaterite and slows the crystallisation of calcite as the presence of strongly hydrated Mg^{2+} ions in ACC retards its dehydration and decreases its solubility [39]. Therefore, due to lower solution supersaturation, slower surface controlled calcite growth is favoured over more rapid nucleation dominated vaterite crystallisation [39]. The presence of Mg^{2+} stabilises the ACC phase causing it to persist for over 10 mins before direct transformation to calcite as the reaction product [39, 42] (also observed in this study). The observed reaction pathway also did not change with increased initial Sr^{2+} / Me^{2+} ratios. The maximum initial Sr^{2+} / Me^{2+} ratio was 0.1, therefore, the upper limit for Sr^{2+} incorporation was not tested in the high-Mg experiments.

Controls on Sr^{2+} uptake during the ACC-vaterite-calcite transformation (Mg-free experiments)

ACC is a highly hydrated and amorphous gel-like precipitate containing water nano-clusters in a disordered Ca^{2+}-CO_3^{2-} framework [54]. In addition, ACC has a very high surface area in comparison

to more crystalline calcium carbonate polymorphs (ACC = 50-400 $m^2\ g^{-1}$ vs. calcite = 0.1-0.5 $m^2\ g^{-1}$) [55], and can therefore, readily adsorb and accommodate elements with ionic radius greater than Ca^{2+}, such as Sr^{2+}, that are generally considered to be less compatible in calcite [21, 34]. Therefore, Sr^{2+} ions are likely to be readily coprecipitated within ACC particles via substitution for Ca^{2+} during formation. The Sr K-edge XANES and EXAFS data collected from Sr-containing ACC samples (Fig. 4) are analogous to Ca K-edge EXAFS spectra collected from ACC samples [56] in that both Me^{2+} cations retain a solution like coordination best fit by ~8 Me-O linkages [57, 58] (SI Table S6) and show no discernible long range ordering using EXAFS analysis. This is similar to Sr K-edge EXAFS spectra from other amorphous phases (e.g. Ca-Si-hydrate; [59]) and is consistent with the sorption of hydrated Sr^{2+} into a disordered coordination environment within ACC.

As a result of rapid non-specific sorption it is expected that Sr^{2+} uptake to ACC phase should be very high (perhaps approaching 100%). However, under the reaction conditions studied, ACC is relatively unstable and almost instantaneously transforms to vaterite (indeed, preparation of vaterite-free ACC samples in the Mg-free experiments was very difficult; see SI Figure S1a). Also, as rapid separation of aqueous samples from the ACC gel was not possible, the calculated Sr distribution coefficients ($K_{d\,Sr}$ = 0.65 ±0.10) determined at the first solution sampling point after 5 min represented experiments where vaterite was already the dominant phase present (i.e. the $K_{d\,Sr}$ relates to Sr^{2+} incorporation to vaterite, not ACC). EXAFS data from samples recovered after just 1 min reaction time also provide evidence for Sr-C and Sr-Ca bond distances consistent with very rapid Sr^{2+} incorporation into vaterite [31]. When incorporated into vaterite the result from this and previous studies [4] indicate Sr^{2+} retains a larger 8-fold Sr-O coordination environment, ($K_{d\,Sr}$ = 1.19; [60]) and is expected to be relatively compatible in the vaterite structure [31]. Therefore, the high $K_{d\,Sr}$ values observed in these experiments after 5 minute can be explained by rapid nucleation of vaterite growth from the ACC precursor.

$K_{d\,Sr}$ does not change significantly (within error) during the transformation to calcite in experiments performed at [Me^{2+}] = 1 mol L^{-1} (Fig. 2a). The maintenance of high $K_{d\,Sr}$ values during the

vaterite to calcite transformation is unexpected. The larger Sr^{2+} ion is considered incompatible in calcite [21] and therefore is predicted to be rejected from the calcite lattice during this transformation, producing a downward trend in $K_{d\,Sr}$ over time. However, the relationship between higher $K_{d\,Sr}$ and higher calcite precipitation rates is well known [20, 24, 27, 29, 52], suggesting a kinetic control for higher Sr^{2+} uptake. The final $K_{d\,Sr}$ values observed in calcite from ACC crystallisation experiments (0.44-0.74; Fig. 2c) exceed both equilibrium growth experiments (0.02-0.05; [20]), and rapid growth crystallisation experiments (0.10-0.40; [24, 29, 52]), but are similar to $K_{d\,Sr}$ values observed in some biological mediated processes (0.50-0.80; [31, 52]) where ACC transformation and rapid calcite nucleation is the most likely mechanism of calcite precipitation.

Under the reaction conditions studied, the transformation of vaterite to calcite follows the Ostwald step rule [61] relating primarily to the solubility difference between vaterite and calcite [37]. The maximum rate of calcite precipitation is therefore expected in experiments where the rate of vaterite dissolution is high and the instantaneous $[Ca^{2+}]$ approaches equilibrium concentrations with respect to vaterite (i.e. at equilibrium, the vaterite dissolution rate = the calcite precipitation rate). This condition is most easily met in crystallisation experiments using high ionic strength solutions ($[Me^{2+}]$ = > 1 mol L^{-1}), where a greater mass of vaterite product will be precipitated. Conversely, in lower ionic strength experiments ($[Me^{2+}]$ = < 1 mol L^{-1}), less vaterite will precipitate, producing lower dissolution rates, lower supersaturation with respect to calcite and slower net calcite precipitation rates. This effect explains why the observed trend in $K_{d\,Sr}$ values measured at 24 hours vary proportionally with respect to the initial $[Me^{2+}]$ used (Fig 2c). Thus, although the high supersaturation with respect to calcite, which occurs during precipitation via the ACC route, explains the generally high $K_{d\,Sr}$ values observed; the overall degree of supersaturation (i.e. the ionic strength of the initial solution) is also important in producing greater mass of solid product and higher Sr^{2+}-uptake in the end-product calcite produced.

Sr^{2+} speciation in calcite produced via ACC-vaterite-calcite transformation (Mg-free experiments)

Calcite unit cell volume data from the Mg-free experiments (calculated from the shift in the calcite (100) peak to lower 2θ values; Fig. 5) show that the calcite unit cell expands proportionally as more Sr^{2+} is incorporated (Fig 5a; SI Table S7). The magnitude of lattice expansions observed are in agreement with previous data [21], and taken together with lack of other phases in XRD and SEM analysis, provide strong evidence that Sr^{2+} is truly incorporated into the calcite lattice and is not hosted in other low abundance phases not detected during the analysis.

At lower Sr loadings (Sr^{2+} / Me^{2+} < 0.01 in the initial solution) Sr^{2+} K-edge XANES and EXAFS spectra (Table 3; Fig. 3 & 4) show that Sr adopts a 6-fold coordination in the calcite end product. The EXAFS fits to these neoformed Sr-calcite phases are identical to those reported from a range of natural and precipitated calcite samples (SI Table S6), however, the amount of Sr incorporated is relatively high (~0.6 mol% $SrCO_3$) compared to natural samples (SI Table S7).

At higher Sr-loading (Sr^{2+} / Me^{2+} < 0.01 in the initial solution) Sr^{2+} is retained in a 9-fold coordination in the calcite product. This coordination environment with a longer Sr-O 1st shell distance relative to low Sr-calcite (2.55 ±0.03 Å), and a shorter Sr-C 2nd shell distance relative to low Sr-calcite (3.1 ±0.1 Å), is very similar to the short range coordination environment of Sr^{2+} incorporated into aragonite or vaterite; but the longer Sr-Ca 3rd shell distance (4.10 ±0.05 Å) is equivalent to that found in low Sr-calcite [23, 31]. Increased Debye-Waller factors, reduced occupancy and lack of a resolvable second Sr-Ca shell at ~5 Å also suggest that this Sr^{2+} incorporation site is highly disordered, probably as a result of rapid crystal growth rates (see discussion above). This suggests that at higher Sr^{2+} loadings (~6% mol% $SrCO_3$ was achieved in these experiments) there is an upper limit to Sr^{2+} incorporation in the 6-fold coordinated Ca^{2+} site in calcite. At higher loadings, Sr^{2+} incorporation still occurs, but only by occupying a distorted lattice site that is aragonite-like in its immediate coordination environment but still calcite-like at longer distances. This data, therefore, for the first time demonstrates that Sr^{2+} can adopt a disordered 9-fold coordinate site in calcite, overcoming the

tendency for Sr^{2+} to be rejected from the 6-fold coordinate calcite lattice (such as occurs at lower crystal growth rates). However, this incorporation mechanism is likely to be limited to calcite precipitated at high crystal growth rates such as those inherently associated with ACC transformation to calcite, via vaterite.

Controls on Sr^{2+} uptake during the ACC-calcite transformation (high-Mg experiments)

There is a significant difference in $K_{d\,Sr}$ between the Mg-Free experiments and the high-Mg experiments (Fig. 2a), which consistently produce greater Sr^{2+} uptake ($K_{d\,Sr}$ = 0.90-0.97; approaching 100% Sr^{2+} sorption). ACC is stabilised by the presence of Mg^{2+} ions (incorporation of Mg^{2+} increases the kinetic energy barrier for calcite nucleation and growth as Mg^{2+} ions are more strongly hydrated than Ca^{2+} ions [62, 63]). In similar high-Mg experiments, the ACC phase was stabilised for over 10 mins [39]. Therefore, at the first solution sampling time point in these experiments (5 mins), the measured $K_{d\,Sr}$ represents that due to Sr^{2+} incorporation into ACC. It is unlikely that sorption and incorporation of Sr^{2+} to ACC is favoured in the presence of high concentrations of Mg^{2+} (it is hard to conceive of how the presence of Mg^{2+} would influence Sr^{2+} behaviour in an amorphous gel-like phase containing abundant sorption sites). This suggests that the stabilising effect of Mg^{2+} ions within ACC allows the measurement of a $K_{d\,Sr}$ value in a system approaching equilibrium with ACC (i.e. the longer the ACC phases persists, the greater propensity for Sr^{2+} to remain incorporated into the metastable phase). The presence of strongly hydrated Mg^{2+} ions in ACC inhibits the rapid formation of vaterite [40] and eventually calcite nucleates at multiple sites [51], producing the initially spherical calcite aggregates observed in SEM images (Fig. 1). The crystal grow rates during the ACC-calcite transformation are driven by the very large difference in solubility between these two phases and are extremely rapid (and also significantly exceed those reported for the ACC-vaterite, or vaterite-calcite transformation) [39]. It is not surprising, therefore, that the initially high $K_{d\,Sr}$ observed for the ACC phases are therefore

retained in the calcite produced; and there is much less sensitivity to variation in the initial [Me^{2+}] in these experiments (Fig. 2c).

In the high-Mg experiments, the Sr^{2+} coordination environment determined via EXAFS analysis was best fitted by the same distorted 9-fold coordinated calcite site found at high Sr^{2+} loadings for the Mg-free samples (see discussion above). However, in the high-Mg samples this coordination environment is also adopted at only modest Sr^{2+} loading (~0.09 mol% $SrCO_3$ at the lowest Sr loading) as well as at the intermediate and highest Sr-loadings used (~0.9 and 10 mol% $SrCO_3$). This again suggests that this coordination geometry is only adopted at very high crystal growth rates, and that the growth rates occurring in the high-Mg experiments are sufficiently fast that the normal 6-fold Sr^{2+}-coordination in calcite is not achieved even at modest Sr^{2+}-loadings. Previous arguments regarding the stabilisation of Sr^{2+} incorporation into calcite by Mg^{2+} have centred around the notation that the larger Sr^{2+} ion is balanced by inclusion of smaller Mg^{2+} ions at a certain ratio [26] such that the overall strain in the crystal lattice is reduced and $K_{d\,Sr}$ values are higher compared to Mg-free calcite [45]. Inclusion of smaller Mg^{2+} ions in calcite produces a large reduction in unit cell volume compared to the Mg-free calcite (i.e. causing a shift in the calcite (100) peak to higher 2θ values; as seen at the lowest Sr-loading in Fig. 5). Logic dictates that inclusion of progressively more Sr^{2+} ions should result in increasing unit cell volume. However, in our experiments, increasing Sr-loading also led to increased Mg^{2+} incorporation into the calcite product (from $\sim 3 \rightarrow \sim 5$ mol% $MgCO_3$; SI Table S7). As changes in Mg^{2+} incorporation cause a larger lattice volume effect relative to Sr^{2+} incorporation [26], this effect may explain the overall lattice volume reduction with increasing Sr-loading. However, the observed change in lattice volume is not fully explained by a simple linear combination of Sr^{2+} and Mg^{2+} ion size effects (SI Figure S4), most likely due to the non-crystallographic incorporation of Sr^{2+} and distortion of the calcite structure. Detailed molecular simulations of Mg^{2+} and Sr^{2+} incorporation are, therefore, likely to be required to fully explain the crystal structure of the Mg-Sr-calcite formed by ACC transformation.

Conclusions

Precipitation of calcite via an ACC precursor phase offers a viable route for achieving high Sr^{2+} uptake to solids. In the Sr^{2+}-Ca^{2+}-CO_3^{2-} system the reaction proceeded via the ACC → vaterite → calcite pathway and was complete within 24 hours. High Sr distribution coefficients of 0.44-0.74 were determined and are attributed to high crystal growth rates during the ACC to calcite transformation. At low to intermediate concentrations, Sr^{2+} adopted a 6-fold coordination environment when substituting for Ca^{2+} in the calcite lattice, but at the highest loading used, Sr^{2+} was incorporated in a disordered 9-fold coordination geometry. In the Mg^{2+}-Sr^{2+}-Ca^{2+}-CO_3^{2-} system the observed crystallisation pathway was ACC → calcite, and was accompanied by higher average Sr distribution coefficients of 0.94 ±0.03 due to strongly hydrated Mg^{2+} ions stabilising the ACC phase, which promoted rapid nucleation-mediated growth of calcite and as a result, greater Sr^{2+} sorption and incorporation. After crystallisation, Sr^{2+} was incorporated in a disordered 9-fold coordination geometry in all calcite samples. This was attributed to rapid crystal growth rates preventing incorporation in the smaller 6-fold Ca^{2+} site. This was aided by presence of smaller Mg^{2+} ions balancing the large Sr^{2+} ions in the calcite structure, which also favoured the 9-fold coordination so that overall lattice strain was reduced. Although most scenarios where Sr^{2+} is present as a contaminant (e.g. as radioactive $^{90}Sr^{2+}$) will involve relatively low Sr^{2+} concentrations, the rapid uptake kinetics and higher removal efficiencies (especially when Mg^{2+} is also present) offered by ACC precipitation make this method attractive for removal of Sr contamination and waste minimisation.

Associated Content

Supporting Information.

The Supporting Information is available free of charge on the ACS Publications website at DOI: XXXXXXXXXXXX. Additional tables of experimental conditions, Detailed XAS methodology and EXAFS standards data, example XRD patterns, supporting data for Sr^{2+} and Mg^{2+} uptake to solids and unit cell calculations.

Author information

Corresponding Author* E-mail: i.t.burke@leeds.ac.uk.

Notes: The authors declare no competing financial interests.

Acknowledgements

This work was supported by a PhD Bursary from the UK Nuclear Decommissioning Authority to JLL, and, beamtime awards at Beamline B18 at the Diamond Light source, UK, and the Dubble Beamline at the European Synchrotron Radiation Source, France.

REFERENCES

1. de Villiers, S., M. Greaves, and H. Elderfield, An intensity ratio calibration method for the accurate determination of Mg/Ca and Sr/Ca of marine carbonates by ICP - AES. Geochemistry, Geophysics, Geosystems, 2002. **3**.
2. Morse, J.W., Q. Wang, and M.Y. Tsio, Influences of temperature and Mg: Ca ratio on CaCO3 precipitates from seawater. Geology, 1997. **25**: p. 85-87.
3. Schrag, D.P., Rapid analysis of high-precision Sr/Ca ratios in corals and other marine carbonates. Paleoceanography, 1999. **14**: p. 97-102.
4. Fairbanks, R.G., et al., Radiocarbon calibration curve spanning 0 to 50,000 years BP based on paired 230 Th/234 U/238 U and 14 C dates on pristine corals. Quaternary Science Reviews, 2005. **24**: p. 1781-1796.
5. Richards, D.A., et al., U-Pb dating of a speleothem of Quaternary age. Geochimica et Cosmochimica Acta, 1998. **62**: p. 3683-3688.

6. Fujita, Y., et al., Strontium incorporation into calcite generated by bacterial ureolysis. Geochimica et Cosmochimica Acta, 2004. **68**: p. 3261-3270.

7. Warren, L.A., et al., Microbially mediated calcium carbonate precipitation: implications for interpreting calcite precipitation and for solid-phase capture of inorganic contaminants. Geomicrobiology Journal, 2001. **18**: p. 93-115.

8. Fujita, Y., et al., Stimulation of microbial urea hydrolysis in groundwater to enhance calcite precipitation. Environmental science & technology, 2008. **42**: p. 3025-3032.

9. Hodkin, D.J., et al., Coprecipitation of 14C and Sr with carbonate precipitates: The importance of reaction kinetics and recrystallization pathways. Science of The Total Environment, 2016. **562**: p. 335-343.

10. Katsikopoulos, D., et al., Co-crystallization of Co (II) with calcite: Implications for the mobility of cobalt in aqueous environments. Chemical Geology, 2008. **254**: p. 87-100.

11. Wallace, S.H., et al., Effect of groundwater pH and ionic strength on strontium sorption in aquifer sediments: implications for 90 Sr mobility at contaminated nuclear sites. Applied Geochemistry, 2012. **27**: p. 1482-1491.

12. McKinley, J.P., et al., Cation exchange reactions controlling desorption of 90 Sr 2+ from coarse-grained contaminated sediments at the Hanford site, Washington. Geochimica et Cosmochimica Acta, 2007. **71**: p. 305-325.

13. Lam, R.S., et al., Synthesis-dependant structural variations in amorphous calcium carbonate. CrystEngComm, 2007. **9**: p. 1226-1236.

14. Plummer, L.N. and E. Busenberg, The solubilities of calcite, aragonite and vaterite in CO 2-H 2 O solutions between 0 and 90 C, and an evaluation of the aqueous model for the system CaCO 3-CO 2-H 2 O. Geochimica et Cosmochimica Acta, 1982. **46**: p. 1011-1040.

15. Markgraf, S.A. and R.J. Reeder, High-temperature structure refinements of calcite and magnesite. American Mineralogist, 1985. **70**: p. 590-600.

16. Bots, P., et al., The role of SO4 in the switch from calcite to aragonite seas. Geology, 2011. **39**: p. 331-334.

17. Demichelis, R., et al., The multiple structures of vaterite. Crystal Growth & Design, 2013. **13**: p. 2247-2251.

18. Mugnaioli, E., et al., Ab initio structure determination of vaterite by automated electron diffraction. Angewandte Chemie International Edition, 2012. **51**: p. 7041-7045.

19. Kabalah-Amitai, L., et al., Vaterite crystals contain two interspersed crystal structures. Science, 2013. **340**: p. 454-457.

20. Tesoriero, A.J. and J.F. Pankow, Solid solution partitioning of Sr2+, Ba2+, and Cd2+ to calcite. Geochimica et Cosmochimica Acta, 1996. **60**: p. 1053-1063.

21. Matsunuma, S., et al., Doping Incompatible Elements into Calcite through Amorphous Calcium Carbonate. Crystal Growth & Design, 2014. **14**: p. 5344-5348.

22. Pingitore, N.E., et al., Mode of incorporation of Sr2+ in calcite: Determination by X-ray absorption spectroscopy. Geochimica et Cosmochimica Acta, 1992. **56**: p. 1531-1538.

23. Finch, A.A., et al., Strontium in coral aragonite: 1. Characterization of Sr coordination by extended absorption X-ray fine structure. Geochimica et Cosmochimica Acta, 2003. **67**: p. 1197-1202.

24. Nehrke, G., et al., Dependence of calcite growth rate and Sr partitioning on solution stoichiometry: Non-Kossel crystal growth. Geochimica et Cosmochimica Acta, 2007. **71**: p. 2240-2249.

25. Lemarchand, D., G. Wasserburg, and D. Papanastassiou, Rate-controlled calcium isotope fractionation in synthetic calcite. Geochimica et Cosmochimica Acta, 2004. **68**: p. 4665-4678.

26. Mucci, A. and J.W. Morse, The incorporation of Mg2+ and Sr2+ into calcite overgrowths: influences of growth rate and solution composition. Geochimica et Cosmochimica Acta, 1983. **47**: p. 217-233.

27. Lorens, R.B., Sr, Cd, Mn and Co distribution coefficients in calcite as a function of calcite precipitation rate. Geochimica et Cosmochimica Acta, 1981. **45**: p. 553-561.

28. Tang, J., S.J. Köhler, and M. Dietzel, Sr 2+/Ca 2+ and 44 Ca/40 Ca fractionation during inorganic calcite formation: I. Sr incorporation. Geochimica et Cosmochimica Acta, 2008. **72**: p. 3718-3732.

29. Gabitov, R. and E. Watson, Partitioning of strontium between calcite and fluid. Geochemistry, Geophysics, Geosystems, 2006. **7**(11).

30. Stoll, H.M., et al., Calcification rate and temperature effects on Sr partitioning in coccoliths of multiple species of coccolithophorids in culture. Global and Planetary Change, 2002. **34**: p. 153-171.

31. Brinza, L., et al., Incorporation of strontium in earthworm-secreted calcium carbonate granules produced in strontium-amended and strontium-bearing soil. Geochimica et Cosmochimica Acta, 2013. **113**: p. 21-37.

32. Meldrum, F.C. and H. Cölfen, Controlling mineral morphologies and structures in biological and synthetic systems. Chemical Reviews, 2008. **108**: p. 4332-4432.

33. Raz, S., S. Weiner, and L. Addadi, Formation of high-magnesian calcites via an amorphous precursor phase: possible biological implications. Advanced Materials, 2000. **12**: p. 38-42.

34. Menadakis, M., G. Maroulis, and P.G. Koutsoukos, A quantum chemical study of doped CaCO3 (calcite). Computational Materials Science, 2007. **38**: p. 522-525.

35. Rodriguez-Blanco, J., S. Shaw, and L. Benning, *How to make 'stable'ACC:* protocol and preliminary structural characterization. Mineralogical Magazine, 2008. **72**: p. 283-286.

36. Rodriguez-Blanco, J.D., S. Shaw, and L.G. Benning, The kinetics and mechanisms of amorphous calcium carbonate (ACC) crystallization to calcite, via vaterite. Nanoscale, 2011. **3**: p. 265-271.

37. Bots, P., et al., Mechanistic insights into the crystallization of amorphous calcium carbonate (ACC). Crystal Growth & Design, 2012. **12**: p. 3806-3814.

38. Ogino, T., T. Suzuki, and K. Sawada, The formation and transformation mechanism of calcium carbonate in water. Geochimica et Cosmochimica Acta, 1987. **51**: p. 2757-2767.

39. Rodriguez-Blanco, J.D., et al., The role of pH and Mg on the stability and crystallization of amorphous calcium carbonate. Journal of Alloys and Compounds, 2012. **536**: p. S477-S479.

40. Rodriguez-Blanco, J.D., et al., The role of Mg in the crystallization of monohydrocalcite. Geochimica et Cosmochimica Acta, 2014. **127**: p. 204-220.

41. Rodriguez-Blanco, J.D., S. Shaw, and L.G. Benning, A route for the direct crystallization of dolomite. American Mineralogist, 2015. **100**: p. 1172-1181.

42. Loste, E., et al., The role of magnesium in stabilising amorphous calcium carbonate and controlling calcite morphologies. Journal of Crystal Growth, 2003. **254**: p. 206-218.

43. Sand, K.K., et al., Crystallization of CaCO3 in Water–Alcohol Mixtures: Spherulitic Growth, Polymorph Stabilization, and Morphology Change. Crystal Growth & Design, 2012. **12**: p. 842-853.

44. Tribello, G.A., et al., A molecular dynamics study of the early stages of calcium carbonate growth. The Journal of Physical Chemistry B, 2009. **113**: p. 11680-11687.

45. Bischoff, W.D., F.C. Bishop, and F.T. Mackenzie, Biogenically produced magnesian calcite; inhomogeneities in chemical and physical properties; comparison with synthetic phases. American Mineralogist, 1983. **68**: p. 1183-1188.

46. Brečević, L. and A.E. Nielsen, Solubility of amorphous calcium carbonate. Journal of Crystal Growth, 1989. **98**: p. 504-510.

47. Ravel, B. and M. Newville, ATHENA, ARTEMIS, HEPHAESTUS: data analysis for X-ray absorption spectroscopy using IFEFFIT. Journal of synchrotron radiation, 2005. **12**: p. 537-541.

48. Tenderholt, A., B. Hedman, and K.O. Hodgson, PySpline: a modern, cross-platform program for the processing of raw averaged XAS edge and EXAFS data. X-Ray Absorption Fine Structure--XAFS 13, 2007. **882**: p. 105-107.

49. Tomic, S., et al., New tools for the analysis of EXAFS: the DL EXCURV package. Council for the Central Laboratory of the Research Councils, 2005.

50. Bots, P., et al., Mechanistic Insights into the Crystallization of Amorphous Calcium Carbonate (ACC). Crystal Growth & Design, 2012. **12**: p. 3806-3814.

51. Purgstaller, B., et al., Transformation of Mg-bearing amorphous calcium carbonate to Mg-calcite–In situ monitoring. Geochimica et Cosmochimica Acta, 2016. **174**: p. 180-195.

52. Mitchell, A.C. and F.G. Ferris, The coprecipitation of Sr into calcite precipitates induced by bacterial ureolysis in artificial groundwater: temperature and kinetic dependence. Geochimica et Cosmochimica Acta, 2005. **69**: p. 4199-4210.

53. Parkman, R.H., et al., A study of the interaction of strontium ions in aqueous solution with the surfaces of calcite and kaolinite. Geochimica et Cosmochimica Acta, 1998. **62**: p. 1481-1492.

54. Bushuev, Y.G., A.R. Finney, and P.M. Rodger, Stability and Structure of Hydrated Amorphous Calcium Carbonate. Crystal Growth & Design, 2015. **15**: p. 5269-5279.

55. Kim, Y.-Y., et al., A critical analysis of calcium carbonate mesocrystals. Nat Commun, 2014. **5**.

56. Politi, Y., et al., Structural characterization of the transient amorphous calcium carbonate precursor phase in sea urchin embryos. Advanced Functional Materials, 2006. **16**: p. 1289-1298.

57. Jalilehvand, F., et al., Hydration of the Calcium Ion. An EXAFS, Large-Angle X-ray Scattering, and Molecular Dynamics Simulation Study. Journal of the American Chemical Society, 2001. **123**: p. 431-441.

58. O'Day, P.A., et al., X-ray absorption spectroscopy of strontium(II) coordination. I. Static and thermal disorder in crystalline, hydrated, and precipitated solids and in aqueous solution. Journal of Colloid and Interface Science, 2000. **222**: p. 184-197.

59. Wieland, E., et al., Strontium uptake by cementitious materials. Environmental Science and Technology, 2008. **42**: p. 403-409.

60. Dietzel, M., N. Gussone, and A. Eisenhauer, Co-precipitation of Sr2+ and Ba2+ with aragonite by membrane diffusion of CO2 between 10 and 50 ℃. Chemical Geology, 2004. **203**: p. 139-151.

61. Van Santen, R., The Ostwald step rule. The Journal of Physical Chemistry, 1984. **88**: p. 5768-5769.

62. De Yoreo, J.J., et al., Rethinking Classical Crystal Growth Models through Molecular Scale Insights: Consequences of Kink-Limited Kinetics. Crystal Growth & Design, 2009. **9**: p. 5135-5144.

63. Politi, Y., et al., Role of magnesium ion in the stabilization of biogenic *amorphous calcium carbonate: A structure− function investigation.* Chemistry of Materials, 2009. **22**: p. 161-166.

For Table of Contents Use Only

Manuscript Title: Mechanism of enhanced strontium uptake into calcite via an amorphous calcium carbonate (ACC) crystallisation pathway

Author List: Littlewood, Janice; Shaw, Samuel; Peacock, Caroline; Bots, Pieter; Trivedi, Divyesh; Burke, Ian

TOC Graphic

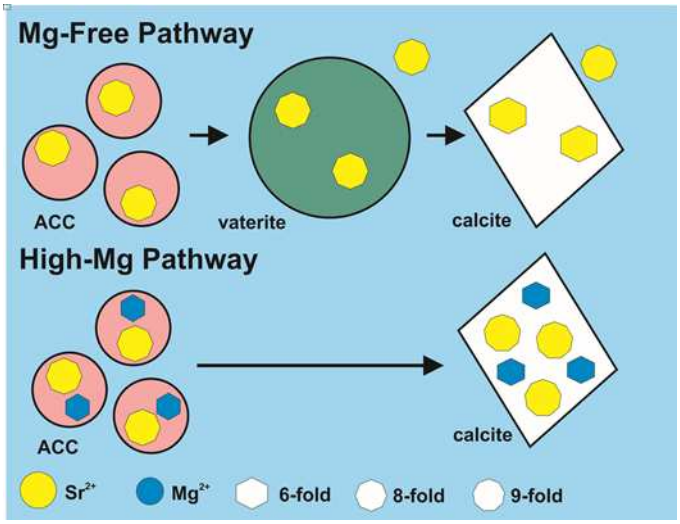

Synopsis

During calcite crystallisation from ACC via vaterite, Sr^{2+} was primarily incorporated into calcite in the 6 fold coordinate Ca^{2+} site. High-Mg concentrations induced direct calcite crystallisation from ACC and Sr^{2+} was incorporated into calcite in a 9-fold coordinate site in all experiments due to rapid crystallisation kinetics and smaller Mg^{2+} ions compensating for larger Sr^{2+} ions in the calcite lattice.